

1  
2  
3  
4  
5  
6  
7  
8  
9  
10  
11  
12  
13  
14  
15  
16  
17  
18  
19  
20  
21  
22

**A Statistically Optimal Analysis of Systematic Differences between Aeolus  
HLOS Winds and NOAA’s Global Forecast System**

Hui Liu<sup>1,2</sup>, Kevin Garrett<sup>1</sup>, Kayo Ide<sup>3</sup>, Ross N. Hoffman<sup>1,2</sup>, and Katherine E. Lukens<sup>1,2</sup>

<sup>1</sup>NOAA/NESDIS/Center for Satellite Applications and Research (STAR), College Park, MD  
20740, USA

<sup>2</sup>Cooperative Institute for Satellite Earth System Studies (CISESS), University of Maryland,  
College Park, MD 20740, USA

<sup>3</sup>University of Maryland, College Park, MD 20740, USA

Correspondence to: Kevin Garrett, NOAA/NESDIS/STAR, 5830 University Research Ct,  
College Park, MD 20740, USA. Email: kevin.garrett@noaa.gov. Phone: (301) 683-3641.

Coauthor contact information:  
Hui Liu: Hui.Liu@noaa.gov, ORCID 0000-0002-7959-0984.  
Kevin Garrett: : kevin.garrett@noaa.gov, ORCID 0000-0002-7444-4363.  
Kayo Ide: Kayo.Ide@noaa.gov, ORCID 0000-0001-5789-9326.  
Ross N. Hoffman: Ross.N.Hoffman@noaa.gov, ORCID 0000-0002-4962-9438.  
Katherine E. Lukens: Katherine.Lukens@noaa.gov.

23

24 **Abstract**

25 The European Space Agency Aeolus mission launched a first-of-its-kind spaceborne Doppler wind  
26 lidar in August 2018. To optimize assimilation of the Aeolus Level-2B (B10) Horizontal Line-of-  
27 Sight (HLOS) winds, significant systematic differences between the observations and numerical  
28 weather prediction (NWP) background winds should be removed. Total least squares (TLS)  
29 regression is used to estimate speed-dependent systematic differences between the Aeolus HLOS  
30 winds and the National Oceanic and Atmospheric Administration (NOAA) Finite-Volume Cubed-  
31 Sphere Global Forecast System (FV3GFS) 6-h forecast winds. Unlike ordinary least squares  
32 regression, TLS regression optimally accounts for random errors in both predictors and  
33 predictands. Large well-defined, speed-dependent systematic differences are found in the lower  
34 stratosphere and troposphere in the tropics and Southern Hemisphere. Correction of these  
35 systematic differences improves the forecast impact of Aeolus data assimilated into the NOAA  
36 global NWP system.

37

38 **Key words:** Aeolus winds, Doppler wind lidar, total least squares bias correction

39

## 40 **1 Introduction**

41           The spaceborne Doppler wind lidar onboard the European Space Agency (ESA) Aeolus  
42 mission measures both Mie (i.e., clouds and aerosols) and Rayleigh (i.e., molecular) backscatter  
43 to derive wind profiles along the sensor’s Horizontal Line of Sight (HLOS) throughout the  
44 troposphere and lower stratosphere [Straume-Lindner, 2018; Straume et al., 2020]. The Aeolus  
45 HLOS Level-2B (L2B) winds have demonstrated positive impacts on global weather forecasts  
46 [Rennie et al., 2021; Cress, 2020; Garrett et al., 2020, 2022].

47           To optimize the positive impact of Aeolus HLOS winds on weather forecasts, large  
48 systematic differences between Aeolus winds and numerical weather prediction (NWP) model  
49 background winds should be corrected [Daley, 1991]. Therefore, it is important to identify  
50 potential systematic differences between Aeolus winds and their NWP model background  
51 counterparts [Liu et al., 2020, 2021]. The systematic differences may come from both the NWP  
52 model background and the Aeolus winds. First, current operational global NWP background winds  
53 still have larger errors or uncertainty in regions where conventional wind observations are sparse  
54 or absent. For example, the 6-h forecast zonal winds from the ECMWF model  
55 (<https://www.ecmwf.int/en/forecasts>) and the NOAA Finite-Volume Cubed-Sphere Global  
56 Forecast System (FV3GFS) model (Kleist et al., 2021) show large systematic differences in the  
57 upper troposphere and lower stratosphere of the tropics, the Southern Hemisphere (SH), and  
58 poleward of 70° N, with maxima on the order of 2.0, -0.5, and 0.5 m/s, respectively (Fig. 1). Such  
59 systematic differences in regions where conventional data are sparse may be due in part to  
60 differences in the assimilation of satellite radiances at the NWP centers. Second, although  
61 corrections to several substantial sources of systematic differences in the Aeolus HLOS winds

62 (baseline B10) have been implemented, including corrections to the dark current signal anomalies  
63 of single pixels (so-called hot pixels) on the Accumulation-Charge-Coupled Devices (ACCDs), to  
64 the linear drift in the illumination of the Mie and Rayleigh spectrometers, and to the telescope M1  
65 mirror temperature variations [Reitebuch et al., 2020; Weiler et al., 2021], uncorrected systematic  
66 differences due to potential calibration issues might remain in Aeolus HLOS winds and may  
67 contribute to potential systematic differences between Aeolus and the NWP background HLOS  
68 winds. The residual systematic differences may lead to sub-optimal assimilation of Aeolus HLOS  
69 winds in NWP systems.

70 For clarity in the remainder of this article certain words and phrases are assigned specific  
71 definitions. Thus, throughout this article, the phrase “**Aeolus winds**” specifically means the  
72 observations of Aeolus Level-2B (B10) HLOS winds. Similarly, the phrase “**FV3GFS winds**”  
73 specifically means the numerical weather prediction (NWP) background HLOS winds evaluated  
74 from the FV3GFS 6-h forecasts at the observation location and time. (In discussions of winds that  
75 are not HLOS winds, terms like  $u$ -wind,  $v$ -wind, or wind vector are used.) Further, the phrase “**Mie**  
76 **winds**” specifically means Aeolus winds derived from Mie backscatter observations and the phrase  
77 “**Rayleigh winds**” specifically means Aeolus winds derived from Rayleigh backscatter  
78 observations. Also, throughout this article, the word “**innovations**” without further qualification  
79 specifically refers to the differences between these Aeolus and FV3GFS winds, and the word  
80 “**bias**” (as well as the phrases “Mie bias” and “Rayleigh bias”) without further qualification  
81 specifically refers to the mean of these innovations, where the sample mean is over some specified  
82 space-time volume for either the Mie or Rayleigh winds.

83           Speed-dependent biases identified and estimated using ordinary least squares (OLS) are  
84 subject to contamination from random errors in Aeolus and/or FV3GFS winds [Frost and  
85 Thompson, 2000], since OLS assumes no errors in the predictor or independent variable, which in  
86 this case would be either the Aeolus or FV3GFS winds, or a combination of the two. In contrast,  
87 total least squares (TLS) regression accounts for errors in both dependent and independent  
88 variables and generates a statistically optimal analysis of the biases [Deming, 1943; Ripley and  
89 Thompson, 1987; Markovsky and Van Huffel, 2007]. For the case of Aeolus and FV3GFS winds,  
90 the use of linear TLS regression [Ripley and Thompson, 1987] finds an optimal estimate of the  
91 true (assumed linear) relationship between Aeolus and FV3GFS winds.

92           In this study, the TLS regression approach is used to estimate biases that depend linearly  
93 on wind speed. The suboptimality of OLS bias estimates is demonstrated by comparison to the  
94 TLS bias estimates, which are treated as “truth” in this study. A bias correction based on the TLS  
95 bias analysis is proposed to optimize Aeolus wind assimilation by the FV3GFS model and thus  
96 improve the impact of Aeolus winds on FV3GFS forecasts. Section 2 describes the Aeolus and  
97 FV3GFS winds, the TLS bias analysis method, and the estimation of the ratio of error variances  
98 of Aeolus to FV3GFS winds, which ratio is used in the TLS regression. Section 3 describes the  
99 variations of the TLS bias estimates with height, latitude, and wind speed. Section 4 demonstrates  
100 the substantial differences between the TLS and OLS bias estimates. Section 5 proposes a TLS  
101 bias correction for Aeolus data assimilation. The forecast impact of the TLS bias correction is  
102 presented in Section 6. Section 7 presents a summary of findings and conclusions.

## 103 2 Data and Methodology

### 104 2.1 Aeolus L2B and FV3GFS background wind data

105 The Aeolus L2B cloudy-sky Mie winds and clear-sky Rayleigh winds are examined for the  
106 period 1-7 September 2019. This one-week period provides a sufficient sample to estimate the  
107 biases. The Aeolus winds were obtained from the Aeolus dataset (baseline B10) re-processed by  
108 ESA [Rennie et al., 2021, Weiler et al., 2021]. The reprocessing includes the M1 bias correction,  
109 which removes most of the globally and vertically averaged biases of both Mie and Rayleigh winds  
110 [Weiler et al., 2021]. The Aeolus winds are reported at a standard set of vertical layers [de Kloe,  
111 2019, 2020]. This study examines Mie and Rayleigh winds within height ranges of 0-22 km that  
112 include nearly all Aeolus winds. The height is defined relative to the EGM96 geoid for the L2B  
113 winds [Tan et al. 2008].

114 The Aeolus and FV3GFS winds are obtained from a data assimilation experiment  
115 (hereafter the BASE experiment) where the Aeolus winds are monitored and the Aeolus wind  
116 observation operator ( $H_i$ ) is applied to the FV3GFS background ( $\mathbf{x}^b$ ) to obtain the value of  
117 FV3GFS wind ( $y_i^b = H_i(\mathbf{x}^b)$ ) corresponding to each Aeolus wind ( $y_i^o$ ). This experiment employs  
118 the FV3GFS data assimilation system, called Global Statistical Interpolation [GSI, Kleist et al.  
119 2009], configured for the 4DEnVar algorithm with 64 vertical levels, and horizontal resolutions of  
120 C384 (~25 km) for the deterministic analysis and forecast and C192 (~50 km) for the 80 ensemble  
121 members [Wang and Lei, 2014].

122 Similar Aeolus data quality control procedures as recommended by ESA and ECMWF  
123 [Rennie et al., 2021] were implemented to reject the following observations: HLOS L2B

124 confidence flag “invalid”; Rayleigh winds at layers below 850 hPa, L2B uncertainties greater than  
125 12 m/s, accumulation lengths less than 60 km, and atmospheric pressure within 20 hPa of  
126 topographic surface pressure; Mie winds with L2B uncertainties greater than 5 m/s and  
127 accumulation lengths less than 5 km. Further, a standard outlier check rejects any Aeolus wind for  
128 which  $|y_i^o - y_i^b|$  is greater than 4 times the estimated errors for Aeolus winds prescribed by the  
129 data assimilation system.

130         When examining Aeolus wind statistics, we stratify the Aeolus data by orbital phase, either  
131 ascending when the spacecraft is moving northward or descending when the spacecraft is moving  
132 southward. The vertical and daily variations Mie and Rayleigh biases for global horizontal samples  
133 are consistent throughout the period (Fig. 2). For ascending orbits, the Mie biases are positive  
134 above 6 km and negative below 6 km, and are as large as +1.8 m/s and -0.5 m/s, respectively. The  
135 Mie biases are smaller and positive at most levels in descending orbits. In descending orbits, the  
136 Rayleigh biases are as positive as +1.2 m/s above 10 km, and as negative as -1.2 m/s below 8 km.  
137 The positive biases in ascending orbits are smaller. The results indicate that the biases vary  
138 substantially with height and orbit phase for both Mie and Rayleigh winds. The Mie and Rayleigh  
139 biases also vary considerably with latitude (Fig. 3). Mie biases are as positive as +1.5 m/s in the  
140 upper troposphere and Rayleigh biases are as positive as +2.0 m/s in the tropical upper troposphere.  
141 Both Mie and Rayleigh biases are as negative as -1.0 m/s in the lowest layers.

142         The statistical relationship between Aeolus and FV3GFS winds is illustrated by the density  
143 plots in Fig. 4. There is a strong correlation of 0.93 between Mie and FV3GFS winds, and of 0.96  
144 between Rayleigh and FV3GFS winds. The average and OLS regression of the innovations as a  
145 function of Aeolus wind suggest considerable speed-dependent biases with both linear and non-

146 linear components (Fig. 5). In this study, we focus on the estimation and correction of the linear  
 147 part of the biases using the TLS linear regression.

## 148 2.2 TLS Linear Regression

149 In this section, we review the TLS linear regression method [Ripley and Thompson, 1987]  
 150 in the context of estimating potential speed-dependent biases. The TLS estimate for each  
 151 collocated pair of Aeolus and FV3GFS winds ( $y_i^o, y_i^b$ ) is defined by

$$152 \quad y_i^o = \hat{y}_i^o + \varepsilon_i^o \quad \text{and} \quad y_i^b = \hat{y}_i^b + \varepsilon_i^b \quad (i=1, N) \quad (1)$$

153 where  $\hat{y}_i^o$  and  $\hat{y}_i^b$  are the TLS estimates of the true Aeolus and FV3GFS winds,  $\varepsilon_i^o$  and  $\varepsilon_i^b$  are  
 154 random errors, and  $N$  is the number of Aeolus/FV3GFS wind collocations in the sample. The  
 155 sample might be defined by a vertical layer or a latitude band. In OLS regression, since it is  
 156 assumed that there are no errors in the predictor, the predictor can be used directly to estimate the  
 157 predictand. The situation is a little more complicated in TLS regression where  $(\hat{y}_i^b, \hat{y}_i^o)$ , the most  
 158 probable true state, is the point on the regression line that is closest in a statistical sense to the point  
 159  $(y_i^b, y_i^o)$ .

160 Here it is assumed that  $\varepsilon_i^o$  and  $\varepsilon_i^b$  are independent and that the random error variance  
 161 ratio  $\delta = (\sigma^o / \sigma^b)^2 = E[\varepsilon_i^o \varepsilon_i^o] / E[\varepsilon_i^b \varepsilon_i^b]$  is known. The error variance ratio  $\delta$  is a crucial  
 162 parameter in determining the TLS bias analysis and is estimated as described in the next section.  
 163 Further, the true relationship between the Aeolus and FV3GFS winds is assumed to be described  
 164 by a linear function (as seen in Fig. 5):

$$165 \quad \hat{y}_i^o = c_0 + c_1 \hat{y}_i^b \quad (i=1, N) \quad (2)$$

166 where  $c_0$  is an offset or constant coefficient and  $c_1$  is a speed-dependent coefficient.

167 The TLS regression finds an optimal estimate of the  $\hat{y}_i^b$ ,  $c_0$  and  $c_1$  by minimizing the cost  
168 function J:

$$\begin{aligned} 169 \quad J &= \sum_{i=1}^N \left( (\varepsilon_i^o / \sigma^o)^2 + (\varepsilon_i^b / \sigma^b)^2 \right) \\ 170 \quad &= \frac{1}{(\sigma^o)^2} \sum_{i=1}^N \left( (y_i^o - c_0 - c_1 \hat{y}_i^b)^2 + \delta (y_i^b - \hat{y}_i^b)^2 \right) \end{aligned} \quad (3)$$

171 To determine the  $\hat{y}_i^b$ , the derivative of J with respect to  $\hat{y}_i^b$  is set to zero:

$$172 \quad \hat{y}_i^b = (c_1 (y_i^o - c_0) + \delta y_i^b) / (c_1^2 + \delta) \quad (i=1, N) \quad (4)$$

173 Eq. (4) thereby reduces the problem to a minimization in terms of  $c_0$  and  $c_1$ . A similar equation  
174 holds even if the error variances vary with  $i$ , but then there is no closed form solution for  $c_0$  and  
175  $c_1$ , as there is in the current case, which is known as the Deming problem [Ripley and Thompson,  
176 1987]. When the coefficients  $c_0$  and  $c_1$  are obtained, the TLS estimate for the new or within-sample  
177 observation is given by Eq. (4). Finally, the estimate of the bias for the  $k$ th observation, either for  
178 a new or within-sample observation, is given by

$$179 \quad \hat{d}_k = \hat{y}_k^o - \hat{y}_k^b = c_0 + (c_1 - 1) \hat{y}_k^b \quad (5)$$

180 Given the form of Eq. (5), we will refer to  $c_0$  and  $(c_1 - 1)$  as the offset and speed-dependent bias  
181 coefficients, respectively, hereafter.

### 182 **2.3 Estimation of the random error variance ratio**

183 In this study, errors of Aeolus winds are estimated by the Hollingsworth-Lonnberg  
184 method (Hollingsworth and Lonnberg, 1986; Garrett et al., 2022), which include Aeolus

185 instrument errors and forward modeling error and representativeness errors of the FV3GFS  
 186 background, at the specific 25 km horizontal resolution. The random error variance ratio  $\delta =$   
 187  $(\sigma^o/\sigma^b)^2$  in the TLS bias analysis is estimated from the innovations from the BASE experiment  
 188 for 1-7 September 2019. It is assumed that there are no correlations between the random errors of  
 189 the Aeolus and FV3GFS winds, and no horizontal correlations between the random errors of  
 190 Aeolus winds separated by more than 90 km. These assumptions are justified *a-posteriori* by the  
 191 reasonable error estimate of FV3GFS background winds (Garrett et al., 2022).

192 Global error estimates are calculated for all Mie and Rayleigh winds in each layer as  
 193 follows. First, the spatial covariance of the innovations is calculated. Since these are innovations  
 194 from the BASE experiment where Aeolus data are not assimilated, it is reasonable to assume that  
 195 the Aeolus and FV3GFS wind errors are uncorrelated. Then the spatial covariance of the  
 196 innovations,  $(\sigma^{o-b})^2$ , at zero separation distance, is equal to

$$197 \quad (\sigma^{o-b})^2 = (\sigma^o)^2 + (\sigma^b)^2 \quad (6)$$

198 where  $\sigma^o$  and  $\sigma^b$  are the random error standard deviations of Aeolus and FV3GFS winds,  
 199 respectively.

200 By assumption, at separation distances greater than 90 km, the innovation covariances are  
 201 estimates of the FV3GFS wind error covariance alone and can be extrapolated back to zero  
 202 separation to get an estimate of the error variance of the FV3GFS winds,  $(\sigma^b)^2$ , and then, using  
 203 Eq. (6), the error variance of the Aeolus winds,  $(\sigma^o)^2$ , may be determined. Note that this can only  
 204 be done using innovation covariances at separation distances large enough to have negligible  
 205 covariances between the Aeolus winds. Since the calculated innovation covariances are globally  
 206 averaged over all HLOS winds, it is not surprising that the corresponding biases are small. The

207 small residual biases in the innovations may introduce small ( $< 0.1$ ) spurious spatial correlations.  
208 This spurious correlation, taken as the value calculated for the last bin (at 990 km), is removed  
209 from the correlation curves at all separation distances. The estimated random error variance ratio  
210  $\delta$  is assigned to the layer center height, defined as the global average heights of the Mie and  
211 Rayleigh wind in each vertical range bin. Fig. 6 shows that the vertical profiles of the square root  
212 of  $\delta$  vary in the range of 1.2-1.6 for Mie winds versus FV3GFS winds and 2-3 for Rayleigh winds  
213 versus FV3GFS winds, respectively.

214 In the future, we plan to explore the benefit of the scene-dependent L2B estimated errors  
215 on the TLS bias estimates and Aeolus wind assimilation.

### 216 **3 The TLS Bias Estimates**

217 In this section, variations of the TLS bias estimates with orbital phase and height are  
218 examined to motivate the use of a TLS bias correction scheme proposed in Section 5.

#### 219 **3.1 Variation of TLS Bias Estimates with Height**

220 The variation of the TLS solution with height and orbital phase is described here. The TLS  
221 samples include winds at all latitudes in each layer. The vertical distribution of the TLS constant  
222 and speed-dependent bias analysis coefficients in Eq. (5) is shown in Fig. 7. The speed-dependent  
223 bias coefficient ( $c_1 - 1$ ) varies substantially with height and orbital phase. For Mie winds, this  
224 coefficient is quite large at most heights, ranging from 3% to 6%, with maxima at 3 km and 12-16  
225 km. For Rayleigh winds, this coefficient is smaller and ranges from 1% to 3% in ascending orbits  
226 and 1-5% in descending orbits, with maxima around the 3.5 km and 16 km.

227 The offset bias coefficient  $c_0$  for both Mie and Rayleigh winds also shows large  
228 variations with height and orbit with its value as large as +/- 1.0 m/s. In general, the offset bias  
229 coefficient is positive in upper layers and negative in layers close to the Earth's surface, consistent  
230 with the patterns seen in the global horizontal average of the innovations in Fig. 2. The vertical  
231 distribution of the average TLS bias estimate as a function of Aeolus wind is shown in Fig. 8. The  
232 biases vary substantially with height. Since the TLS biases are in part dependent on speed, at most  
233 heights the biases increase substantially as the magnitude of Aeolus wind speed increases. The  
234 biases at the extreme Aeolus wind speeds are as large as +2.5 m/s and -1.0 m/s for Mie winds, and  
235 +1.5 m/s and -1.0 m/s for Rayleigh winds. There are clear speed-dependent biases in the vertical  
236 average of these biases as well (Fig. 9). The results suggest that the innovations have both vertically  
237 varying and vertically averaged speed-dependent biases.

### 238 **3.2 Variation of Biases with Latitude**

239 The variation of the TLS solution with latitude and orbital phase is described here. For  
240 this purpose, the samples include all heights in each 10-degree latitude band and the vertical  
241 average of the error ratio  $\delta$  is used. In general, the bias coefficients obtained are large and vary  
242 considerably with latitude and orbital phase, with maxima found in the tropics (Fig. 10). For  
243 example, the speed-dependent bias coefficient ( $c_1 - 1$ ) for Mie winds in the tropics can be quite  
244 large, ranging up to a maximum of 11%. This coefficient is smaller for Rayleigh winds, ranging  
245 from -1% to 5%, with maxima found in the tropics. The offset bias coefficient  $c_0$  for Mie winds  
246 also varies considerably with latitude and orbit, ranging from -1.0 m/s to +1.6 m/s. The offset  
247 bias coefficient  $c_0$  is smaller for Rayleigh winds.

248           The latitudinal distribution of the average TLS bias as a function of Aeolus wind speed is  
249 shown in Fig. 11. For both Mie and Rayleigh winds, the average TLS biases increase considerably  
250 at most latitudes as the magnitude of Aeolus wind speed increases, particularly in the tropics and  
251 SH, with extreme values of about  $\pm 1.5$  m/s.

### 252 **3.3 Discussion**

253           The results indicate that the speed-dependent bias coefficient ( $c_1 - 1$ ) is quite large,  
254 reaching  $\sim 10\%$  and  $5\%$  for Mie and Rayleigh winds, respectively, particularly in the lower  
255 stratosphere and lower troposphere of the tropics. This suggests that there exist large speed-  
256 dependent biases in the FV3GFS and/or Aeolus winds. Given that there exist large uncertainties  
257 in the FV3GFS (and ECMWF) background winds in the tropics (see Fig. 1), it is likely that the  
258 FV3GFS background may be a significant source of the biases, and this will require further  
259 investigation. In any case, these large speed-dependent biases should be corrected to optimize  
260 Aeolus wind assimilation and the impact of Aeolus winds on NWP forecasts. The large variations  
261 of the TLS bias estimates with latitude and height guide the design of the proposed TLS bias  
262 correction in Section 5.

## 263 **4 Comparison to OLS Regressions**

264           Parallel OLS regressions using three different predictors of the biases are compared with  
265 the TLS bias estimate results presented in Section 3. The OLS predictors are the FV3GFS winds,  
266 the Aeolus winds, and their average. The first two of these OLS regressions are equivalent to OLS  
267 regressing Aeolus winds on FV3GFS winds and OLS regressing FV3GFS winds on Aeolus winds.  
268 The regression lines of these two cases are added to Fig. 4. The TLS speed-dependent coefficient

269  $(c_1 - 1)$  (in Eq. 5) is 6% and 4% for Mie and Rayleigh winds, respectively. However, the OLS  
270 regression of Aeolus winds on FV3GFS winds produces considerably smaller bias estimates, with  
271  $(c_1 - 1)$  estimated as 1% and 2% for Mie and Rayleigh winds, respectively. On the other hand,  
272 the OLS regression of the FV3GFS winds on Aeolus winds exhibits much larger bias estimates  
273 relative to the TLS bias analysis, with  $(c_1 - 1)$  estimated as 18% and 15% for Mie and Rayleigh  
274 winds, respectively.

275         The vertical distributions of the average biases as a function of Aeolus winds are shown in  
276 Fig. 12 for the descending orbits for three methods: (1) OLS regression using FV3GFS winds as a  
277 predictor (top row), (2) TLS regression (middle row, which repeats the bottom two panels of Fig.  
278 8), and (3) OLS regression using the average of FV3GFS and Aeolus as a predictor (bottom row).  
279 The average bias estimates in the top panels are about 0.5 m/s smaller in magnitude in most layers  
280 compared to the middle panels. The average biases in the bottom panels are about 0.5-1.0 m/s in  
281 magnitude larger than the middle panels in most layers, particularly for Rayleigh winds. The bias  
282 estimates of OLS regression using Aeolus winds only as a predictor (not shown) are even larger  
283 than what is shown in the bottom panels. The large differences in the bias estimates using the TLS  
284 and OLS regression are due to the fact that both Aeolus and FV3GFS winds have large errors. If  
285 the predictor (either Aeolus or FV3GFS winds) has very small errors, then the OLS regressions  
286 would be close to perfect and the OLS and TLS regressions would give very similar results. In  
287 such situation, the random error ratio would be either infinity small ( $\ll 1$ ) or infinity large ( $\gg 1$ ),  
288 However, the Aeolus and FV3GFS winds have considerable errors, and the actual random error  
289 ratio is about 2-3 for the Rayleigh winds versus FV3GFS winds and about 1.2-1.5 for the Mie  
290 winds versus FV3GFS winds (Fig. 6). This leads to the large differences in the OLS and TLS bias

291 estimates. Specifically, the OLS bias estimates using Aeolus winds as a predictor have larger  
292 differences from the TLS estimates than the OLS estimates using FV3GFS winds as a predictor.

## 293 **5 A TLS Bias Correction**

294 In this section, a TLS bias correction is proposed to optimize Aeolus wind data  
295 assimilation. Because the findings in Section 3 show substantial variation of the bias coefficients  
296 with latitude, vertical layer, and orbital phase, the TLS bias coefficients are calculated from the  
297 winds in 19 discrete bins of latitude (centered every  $10^\circ$  between  $90^\circ$  S to  $90^\circ$  N) for each vertical  
298 range/layer and for ascending and descending orbits separately. The error ratio  $\delta$  shown in Fig. 6  
299 is used in all latitude bands for each layer. For each assimilation cycle, the bias coefficients are  
300 computed by TLS regression for the innovations in the week before the cycle (i.e., for the previous  
301 28 cycles). One week provides a large enough sample for the regression. As shown by Ripley and  
302 Thompson [1987], the TLS solution only involves solving a quadratic equation with coefficients  
303 given by sample sums. Therefore, an efficient approach is to calculate and save these sums for  
304 every cycle and accumulate them over the 28 cycles. For each of the innovations in the assimilation  
305 cycle, values of the TLS regression coefficients  $c_0$  and  $c_1$  are linearly interpolated to the latitude  
306 of the Aeolus observation. Subsequently, the TLS estimated bias, calculated using Eq. (5), is  
307 subtracted from the innovation. Note that the bias correction is determined by the TLS analysis  
308 solution for  $\hat{y}_k^b$  that in turn is determined from the observation and background wind,  $y_k^o$  and  $y_k^b$ ,  
309 following Eq. (4).

310 The proposed scheme is applied to the Aeolus and FV3GFS winds of the BASE  
311 experiment. As expected, the corresponding TLS bias estimates show considerable speed-

312 dependent biases. For example, in the bins centered at the Equator and 80°S, where the speed-  
313 dependent biases are expected to be largest based on Fig. 9, the TLS bias estimates vary  
314 considerably with speed and in some cases are larger in magnitude than 1.5 m/s at higher Aeolus  
315 wind magnitudes (Fig. 13).

316 The vertical distribution of the global average of the remaining biases (i.e., after TLS bias  
317 correction) as a function of Aeolus wind is shown in Fig. 14, which is in the same format and for  
318 the same sample of observations as Fig. 8. A comparison of these two figures reveals that most of  
319 the biases are removed by the proposed TLS bias correction. The latitudinal variations of the biases  
320 are also corrected (Fig. 15). In addition, the biases in the vertical average are also mostly removed,  
321 as shown in Fig. 9.

## 322 **6 Impact of the TLS bias correction on forecast skill**

323 Several Observing System Experiments (OSEs) using the NOAA global data assimilation  
324 system are performed using the Aeolus winds with and without the TLS bias correction. For the  
325 period of 2 August – 16 September 2019, Garrett et al., (2022) demonstrate positive impact of  
326 Aeolus winds on NOAA global forecast. The largest impact is seen in the tropical upper  
327 troposphere and lower stratosphere where the Day 1-3 wind vector forecast RMSE is reduced by  
328 up to 4%. Specifically, the assimilation of Aeolus impacts the steering currents ambient to tropical  
329 cyclones, resulting in up to a 20% reduction in track forecast error in the Eastern Pacific and  
330 Atlantic basins. The application of TLS bias correction increases the positive impact of Aeolus  
331 data assimilation on the forecasts.

332 OSE results for a 2019 record-breaking winter storm case over the US are reported here.  
333 On 26 November 2019, one major storm approached the West Coast of the US from the Eastern  
334 Pacific and produced a record-breaking low pressure of 973 hPa and wind gust of 171 km/h near  
335 the Oregon/California border. Over the next few days, the low merged with the subtropical jet as  
336 it tracked eastward across the US. The combination of cold air, moisture and high winds produced  
337 snow blizzard conditions across the US.

338 As in Garrett et al. (2022), the OSEs include the baseline experiment (BASE) without the  
339 assimilation of Aeolus winds, the experiment AEOM that is identical to BASE except that Aeolus  
340 winds are assimilated, and the experiment AEOT that is identical to AEOM except that it also  
341 includes the TLS bias correction. A difference Summary Assessment Metric (SAM, Hoffman et  
342 al., 2018) is computed for Day 1-7 forecasts in the North America (NA) region of the experiments  
343 validated at 0000 UTC 22-28 November 2019. The SAM illustrates the overall forecast skill by  
344 normalizing the AC and RMSE values for each parameter (temperature, geopotential height, wind,  
345 and relative humidity) and each lead time. Fig. 16 shows that the TLS bias correction improves  
346 the impact of Aeolus winds on the forecasts of wind, temperature, and geopotential height for Day  
347 3-7 and especially for Day 5-7 lead times. The overall improvement of Aeolus winds for AEOM  
348 and AEOT is about 4% and 10%, respectively (above the 95% significance level, Fig. 16c),  
349 illustrating the usefulness of the TLS bias correction.

350 The vertically integrated water vapor transport (IVT) is a useful metric in forecasting  
351 precipitation associated with winter storms (e.g., Lavers et al. 2017). The IVTs of the Day 7  
352 forecast for the experiments validated for 0000 UTC November 27 and 28 are shown in Fig. 17.  
353 Aeolus winds have a strong impact on the locations and intensities of the IVT maxima near the

354 US West Coast and in the Midwest. In general, the IVTs are closer to the ECMWF analyses in  
355 AEOT than in AEOM. As a result, Aeolus winds show strong impact on the locations and  
356 corresponding amounts of precipitation as seen in Fig. 18, and quantified by the Equitable  
357 Threat and BIAS skill scores (<https://www.wpc.ncep.noaa.gov/rgnscr/verify.html>, Wang et al.,  
358 2014), respectively (Fig. 19). Specifically, the precipitation amounts near the West Coast and  
359 the Midwest are much less in AEOT than in BASE and AEOM. The precipitation in the Midwest  
360 also shifts eastward in AEOT, compared to BASE and AEOM (Fig. 18). The precipitation  
361 forecast skills (verified against NCEP precipitation raingauge data analyses) over the contiguous  
362 United States (CONUS) region, that is, the Equitable Threat (location) and BIAS (amount) score  
363 are shown in Fig. 19. The precipitation amount is over-predicted (BIAS score  $> 1.0$ ) in both  
364 BASE and AEOM, but is closer to the analysis (BIAS score closer to 1.0) in AEOT. The  
365 Equitable Threat is larger (with marginal significance level, Fig. 19c) in AEOT than in BASE  
366 and AEOM, indicating the location of precipitation in the forecast is improved in AEOT. These  
367 results suggest potential benefit of the TLS bias correction to precipitation forecasts.

## 368 **7. Summary and Conclusions**

369 In this study a TLS linear regression is used to optimally estimate speed-dependent linear  
370 biases in the Aeolus innovations. The Aeolus and FV3GFS winds for 1-7 September 2019 are  
371 analyzed. Clear speed-dependent linear biases for both Mie and Rayleigh winds are found,  
372 particularly in the lower troposphere and stratosphere of the tropics and Southern Hemisphere. The  
373 largest biases are about 10% and 5% of FV3GFS wind speed and are as large as  $\pm 2.5$  m/s and  
374  $\pm 1.5$  m/s at high Aeolus wind magnitudes for Mie and Rayleigh winds, respectively.

375           It is found that the TLS linear bias estimates are considerably larger than the OLS  
376 regression of Aeolus innovations on FV3GFS winds. However, they are much smaller than the  
377 OLS regression both on Aeolus winds only and on the average of Aeolus and FV3GFS winds. This  
378 is more evident for the Rayleigh winds.

379           The proposed TLS bias correction remove much of the biases in the innovations before  
380 Aeolus wind assimilation. In a companion paper, Garrett et al. [2022] demonstrate that the  
381 application of this TLS bias correction considerably enhances the positive impact of Aeolus winds  
382 on NOAA FV3GFS global and tropical cyclone forecasts for the period of 2 August to 15  
383 September 2019. In this study, it is also demonstrated that the application of the TLS bias  
384 correction improves the impact of Aeolus winds on the forecast of a record-breaking 2019 winter  
385 storm including the associated precipitation over the US. It is expected that the application of the  
386 TLS bias correction can improve and enhance Aeolus data impacts on the analysis and forecast  
387 skill of other NWP systems. It should be noted that the proposed TLS approach presented here  
388 might be applied to other types of observations that have errors typically characterized as a  
389 percentage of the observed value, including quantities related to the concentrations or mass  
390 fractions of chemical species or hydrometeors, or quantities like radio occultation refractivity and  
391 bending angle.

## 392 **Acknowledgments**

393           The authors thank the two anonymous reviewers for their careful and helpful reviews. This  
394 work was supported by the NOAA/NESDIS Office of Projects, Planning, and Acquisition (OPPA)  
395 Technology Maturation Program (TMP), managed by Patricia Weir and Dr. Nai-Yu Wang,  
396 through the Cooperative Institute for Satellites and Earth System Studies (CISESS) at the

397 University of Maryland (Grant NA14NES4320003 and NA19NES4320002). The authors would  
398 like to acknowledge Drs. Michael Rennie and Lars Isaksen (ECMWF) for their comments and  
399 suggestions on the assimilation of Aeolus observations, and Dr. William McCarty with  
400 NASA/GMAO for providing earlier versions of the GSI with Aeolus ingest and observation  
401 operator capability. The Aeolus L2B BUFR data were provided by ECMWF. The scientific results  
402 and conclusions, as well as any views or opinions expressed herein, are those of the author(s) and  
403 do not necessarily reflect those of NOAA or the U.S. Department of Commerce.

## 404 **7 References**

- 405 Cress, A.: Validation and impact assessment of Aeolus observations in the DWD modeling  
406 system. Status report'. *Aeolus NWP Impacts Working Meeting*, Virtual, 2020. Available  
407 at:  
408 [https://www.aeolus.esa.int/confluence/display/CALVAL/Aeolus+NWP+impact+working](https://www.aeolus.esa.int/confluence/display/CALVAL/Aeolus+NWP+impact+working+meeting+2?preview=/12354328/12354463/5_DWD_acress_aeolus_20200617.pdf)  
409 [+meeting+2?preview=/12354328/12354463/5\\_DWD\\_acress\\_aeolus\\_20200617.pdf](https://www.aeolus.esa.int/confluence/display/CALVAL/Aeolus+NWP+impact+working+meeting+2?preview=/12354328/12354463/5_DWD_acress_aeolus_20200617.pdf).
- 410 Daley R.: Atmospheric data analysis. Cambridge University Press, Cambridge, 457 pp., ISBN-13  
411 978-0521458252, 1991
- 412 de Kloe, J. and Coauthors: Aeolus Data Innovation Science Cluster DISC ADM-Aeolus Level-  
413 2B/2C Processor Input/Output Data Definitions Interface Control Document. *Tech. rep.*,  
414 KNMI, Aeolus, DISC, REF: AED-SD-ECMWF-L2B-037, 2020. Available at:  
415 [https://earth.esa.int/eogateway/documents/20142/37627/Aeolus-L2B-2C-Input-Output-](https://earth.esa.int/eogateway/documents/20142/37627/Aeolus-L2B-2C-Input-Output-DD-ICD.pdf)  
416 [DD-ICD.pdf](https://earth.esa.int/eogateway/documents/20142/37627/Aeolus-L2B-2C-Input-Output-DD-ICD.pdf).

417 Deming, W. E.: Statistical adjustment of data, Wiley, NY (Dover Publications edition, 1985).  
418 ISBN 0-486-64685-8, 1943.

419 Frost, C. and Thompson S.: Correcting for regression dilution bias: comparison of methods for a  
420 single predictor variable, *Journal of the Royal Statistical Society, Series A* 163: 173–190.  
421 <https://doi.org/10.1111/1467-985X.00164>, 2000.

422 Garrett, K., Liu, H., Ide, K., Lukens, K., and Cucurull, L.: Updates to Aeolus Impact Assessment  
423 on NOAA global NWP. 2<sup>nd</sup> ESA Aeolus Cal/Val and Science Workshop, Nov 2-6, 2020.  
424 Available at:  
425 [https://www.dropbox.com/s/cd0r1gz7t77gq0g/Kevin\\_Garrett\\_Oral\\_Evaluation\\_of\\_Aeolus.pptx?dl=0](https://www.dropbox.com/s/cd0r1gz7t77gq0g/Kevin_Garrett_Oral_Evaluation_of_Aeolus.pptx?dl=0).  
426

427 Garrett K., H. Liu, K. Ide, R. N. Hoffman, and K. E. Lukens: Optimization and Impact Assessment  
428 of Aeolus HLOS Wind Data Assimilation in NOAA’s Global Forecast System, *Q. J. R. Meteorol. Soc.*, revised, manuscript QJ-21-0307, 2022.

430 Hoffman, R. N., Kumar, K., Boukabara, S., Yang, F., and Atlas, R.: Progress in Forecast Skill at  
431 Three Leading Global Operational NWP Centers during 2015–17 as Seen in Summary  
432 Assessment Metrics (SAMs), *Wea. Forecasting*, **33**, 1661-1679,  
433 <https://doi.org/10.1175/WAF-D-18-0117.1>, 2018.

434 Hollingsworth, A. and Lonnberg, P.: The statistical structure of short-range forecast errors as  
435 determined from radiosonde data. Part I: The wind field. *Tellus*, 38A, Issue 2, p111-136.  
436 <https://doi.org/10.3402/tellusa.v38i2.11707>, 1986

437 Kleist, D. T. and Coauthors: Introduction of the GSI into the NCEP Global Data Assimilation  
438 System. *Wea. Forecasting*, **24**, 1691–1705, <https://doi.org/10.1175/2009WAF2222201.1>,  
439 2009.

440 Kleist, D. T. and Coauthors: NCEP Operational Global Data Assimilation Upgrades: From  
441 Versions 15 through 16'. Special Symposium on Global and Mesoscale Models, Virtual,  
442 Amer. Meteor. Soc., 12.3. Available at:  
443 <https://ams.confex.com/ams/101ANNUAL/meetingapp.cgi/Paper/378554>, 2021.

444 Lavers, D. A., Zsoter E., Richardson D. S., And Pappenberger L.: An Assessment of the  
445 ECMWF Extreme Forecast Index for WaterVapor Transport during Boreal Winter,  
446 *Weather and Forecast*, v32, 1667-1674, doi: 10.1175/WAF-D-17-0073.1, 2017.

447 Liu, H., Garrett, K. Ide, K., Hoffman, R. N., and Lukens, K. E.: Bias correction and Error  
448 Specification of Aeolus Winds for NOAA Global Data Assimilation System. 2<sup>nd</sup> ESA  
449 Aeolus CAL/VAL and Science Workshop, Nov 2-6, 2020. Available at:  
450 [https://www.dropbox.com/s/f518n7n8ouhgwhy/Hui\\_LIU\\_Flash\\_Evaluation\\_update.pdf?](https://www.dropbox.com/s/f518n7n8ouhgwhy/Hui_LIU_Flash_Evaluation_update.pdf?dl=0)  
451 [dl=0](https://www.dropbox.com/s/f518n7n8ouhgwhy/Hui_LIU_Flash_Evaluation_update.pdf?dl=0).

452 Liu H., K. Garrett, K. Ide, R. N. Hoffman, and K. E. Lukens: Impact Assessment of Aeolus Winds  
453 on NOAA Global Forecast, European Geophysical Union general assembly, 19-30 Apr  
454 2021. Available at: <https://meetingorganizer.copernicus.org/EGU21/session/40837>.

455 Marseille, G.-J., de Kloe, J., Marksteiner, U., Reitebuch, O., Rennie, M. & de Haan, S.: (2022)  
456 NWP calibration applied to Aeolus Mie channel winds. *Quarterly Journal of the Royal*  
457 *Meteorological Society*, 1–15. Available from: <https://doi.org/10.1002/qj.4244>, 2022

458 Markovsky I. and Van Huffel S.: Overview of total least squares methods. *Signal Processing*, vol.  
459 87, pp. 2283–2302. doi: 10.1016/j.sigpro.2007.04.004, 2007.

460 Reitebuch, O., Bracci, F., and Lux, O.: Assessment of the Aeolus performance and bias correction  
461 - results from the Aeolus DISC. 2<sup>nd</sup> Aeolus Cal/Val Workshop, Nov. 2020. Available at:  
462 [https://www.dropbox.com/s/m3kjp540otwm171/Oliver\\_Reitebuch\\_Oral\\_Assessment-](https://www.dropbox.com/s/m3kjp540otwm171/Oliver_Reitebuch_Oral_Assessment-Aeolus-DISC.pdf?dl=0)  
463 [Aeolus-DISC.pdf?dl=0](https://www.dropbox.com/s/m3kjp540otwm171/Oliver_Reitebuch_Oral_Assessment-Aeolus-DISC.pdf?dl=0).

464 Rennie, M. P., Isaksen, L., Weiler, F., de Kloe, J., Kanitz, T. and Reitebuch, O.: The impact of  
465 Aeolus wind retrievals on ECMWF global weather forecasts, *Q. J. R. Meteorol. Soc.*, 147,  
466 3555-3586, doi:10.1002/qj.4142, 2021.

467 Ripley, B. D. and Thompson M.: Regression techniques for the detection of analytical bias,  
468 *Analyst*, 112, 377-383. doi: 10.1039/AN987120037, 1987.

469 Straume-Lindner, A. G.: Aeolus Sensor and Product Description'. *Tech. rep.*, European Space  
470 Agency - European Space Research and Technology Centre, The Netherlands. REF: AE-  
471 SU-ESA-GS-000. Available at:  
472 [https://earth.esa.int/eogateway/documents/20142/37627/Aeolus-Sensor-and-Product-](https://earth.esa.int/eogateway/documents/20142/37627/Aeolus-Sensor-and-Product-Description.pdf)  
473 [Description.pdf](https://earth.esa.int/eogateway/documents/20142/37627/Aeolus-Sensor-and-Product-Description.pdf), 2018.

474 Straume, A.G. and coauthors: ESA's Space-Based Doppler Wind Lidar Mission Aeolus First Wind  
475 and Aerosol Product Assessment Results. Edited by D. Liu, Y. Wang, Y. Wu, B. Gross,  
476 and F. Moshary. *EPJ Web of Conferences* 237: 01007,  
477 <https://doi.org/10.1051/epjconf/202023701007>, 2020.

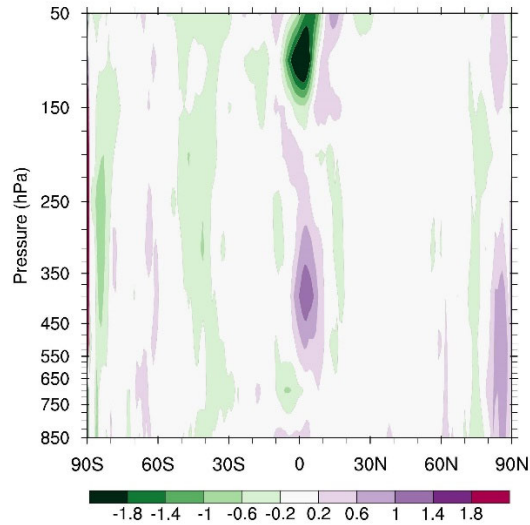
478 Tan, D. G. H. and others: The ADM-Aeolus wind retrieval algorithms, *Tellus A*, 60, 191-205.  
479 doi:10.1111/j.1600-0870.2007.00285.x, 2008.

480 Wang C-C: On the Calculation and Correction of Equitable Threat Score for Model Quantitative  
481 Precipitation Forecasts for Small Verification Areas: The Example of Taiwan, doi:  
482 <https://doi.org/10.1175/WAF-D-13-00087.1>, 788–798, 2014.

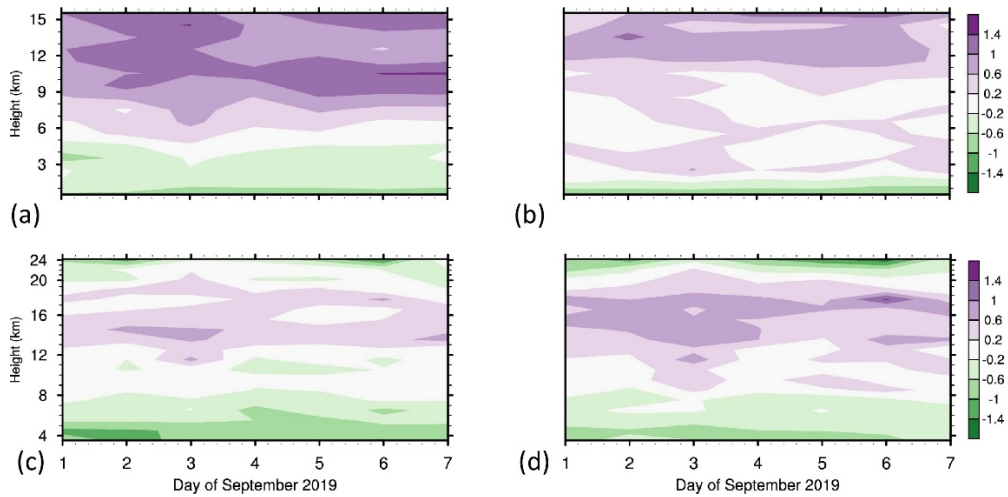
483 Wang, X. and Lei, T.: GSI-Based Four-Dimensional Ensemble–Variational (4DEnsVar) Data  
484 Assimilation: Formulation and Single-Resolution Experiments with Real Data for NCEP  
485 Global Forecast System. *Mon. Wea. Rev.*, **142**, 3303–3325, [https://doi.org/10.1175/MWR-](https://doi.org/10.1175/MWR-D-13-00303.1)  
486 [D-13-00303.1](https://doi.org/10.1175/MWR-D-13-00303.1), 2014.

487 Weiler F. M. Rennie, T. Kanitz, L. Isaksen, E. Checa, Jos de Kloe, O. Reitebuch: Correction of  
488 wind bias for the lidar on-board Aeolus using telescope temperatures, *Atmos. Meas. Tech.*  
489 doi: 10.5194/amt-2021-171, 2021.

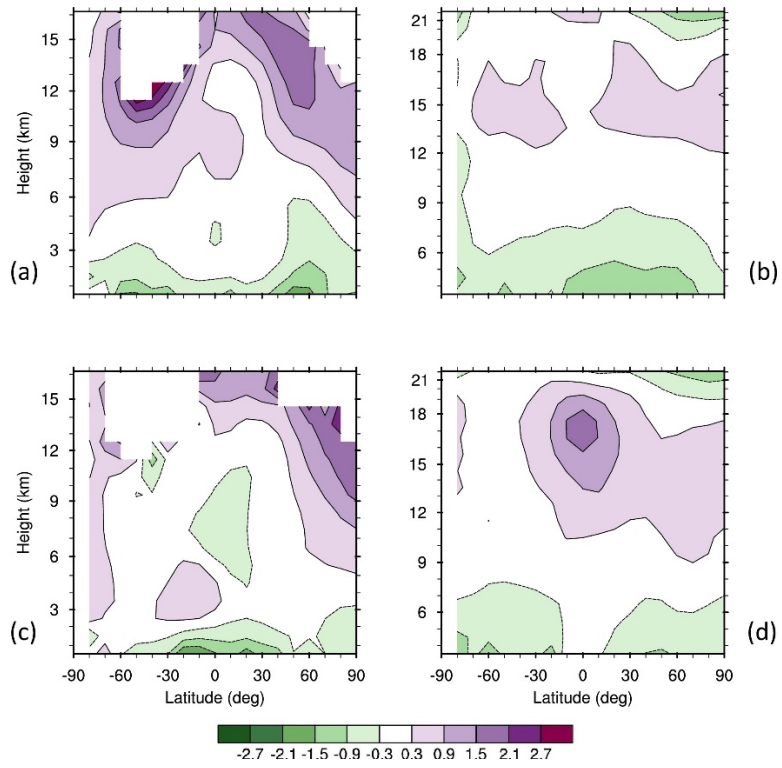
490 **8 Figures**



491  
 492 Figure 1. Zonal and time mean difference of ECMWF minus FV3GFS backgrounds (defined as 6-  
 493 h forecasts) for analysis times 00, 06, 12, and 18 UTC) for zonal wind (m/s). Note that in Figs. 1-  
 494 15 the sample is 1-7 September 2019.



495  
 496 Figure 2. Vertical and daily variations of global horizontal biases (m/s) for Mie winds (a, b) and  
 497 Rayleigh winds (c, d) in ascending (a, c) and descending (b, d) orbits.

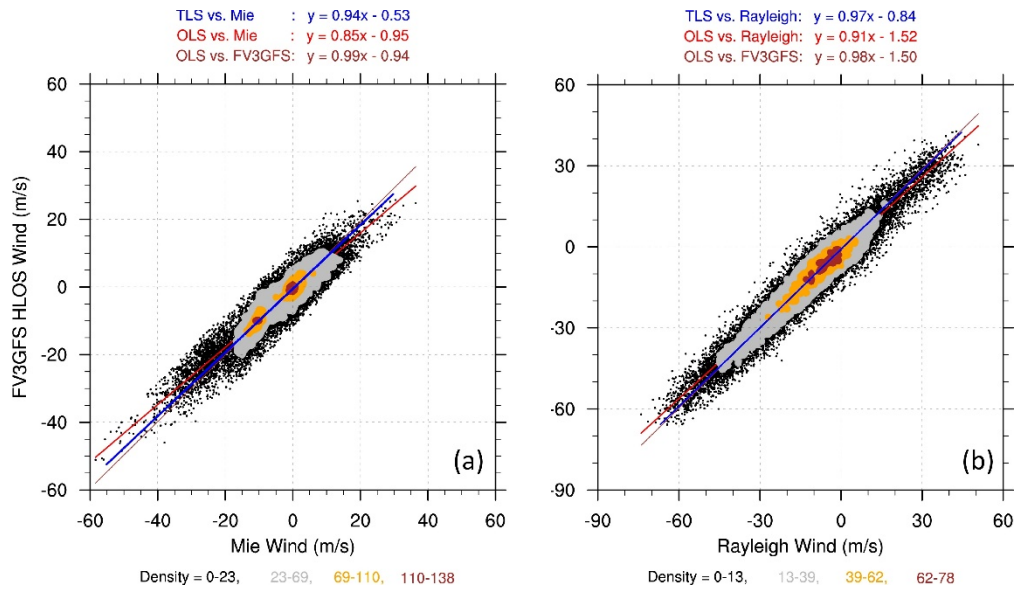


498

499 Figure 3. Latitudinal and height distributions of Mie biases (a, c) and Rayleigh biases (b, d) (color  
 500 scale, m/s) in ascending (a, b) and descending (c, d) orbits.

501

502



503

504 Figure 4. Density plots of global collocated (a) Mie and FV3GFS winds in the layer at ~3.5 km

505 altitude, and (b) Rayleigh and FV3GFS winds in the layer at ~15 km altitude in descending orbits.

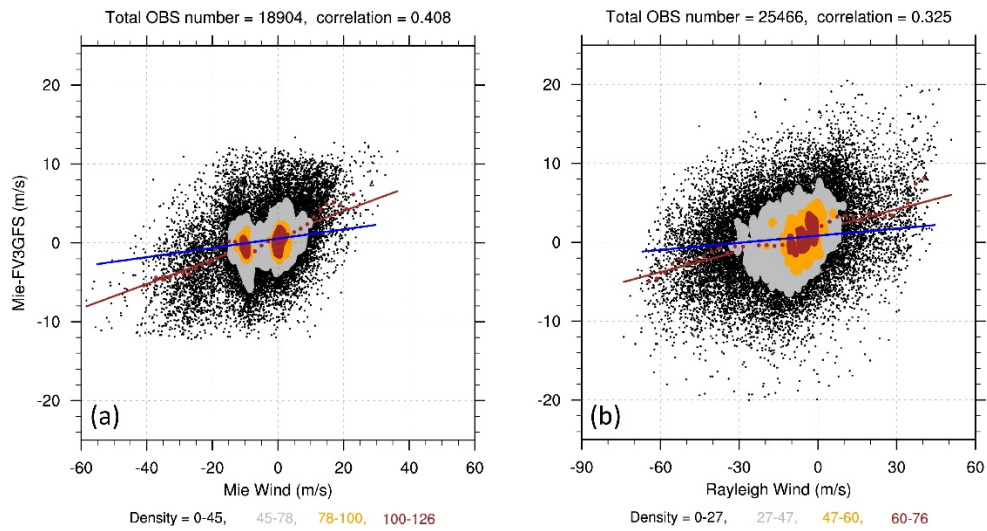
506 The TLS analysis lines (blue), the OLS regression lines of FV3GFS winds on Aeolus winds (red),

507 and the OLS regression lines of Aeolus winds on FV3GFS winds (transformed and plotted as a

508 function of Aeolus winds in brown) are shown, with corresponding regression coefficients

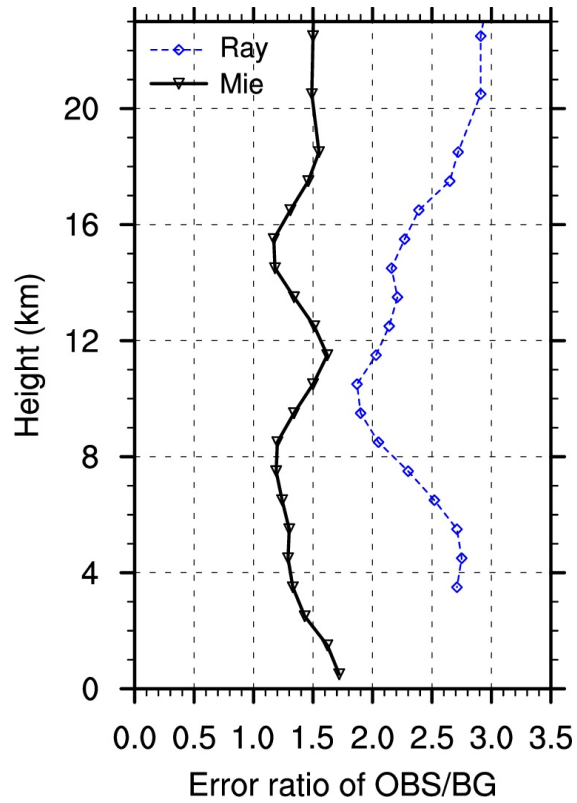
509 displayed above each panel.

510



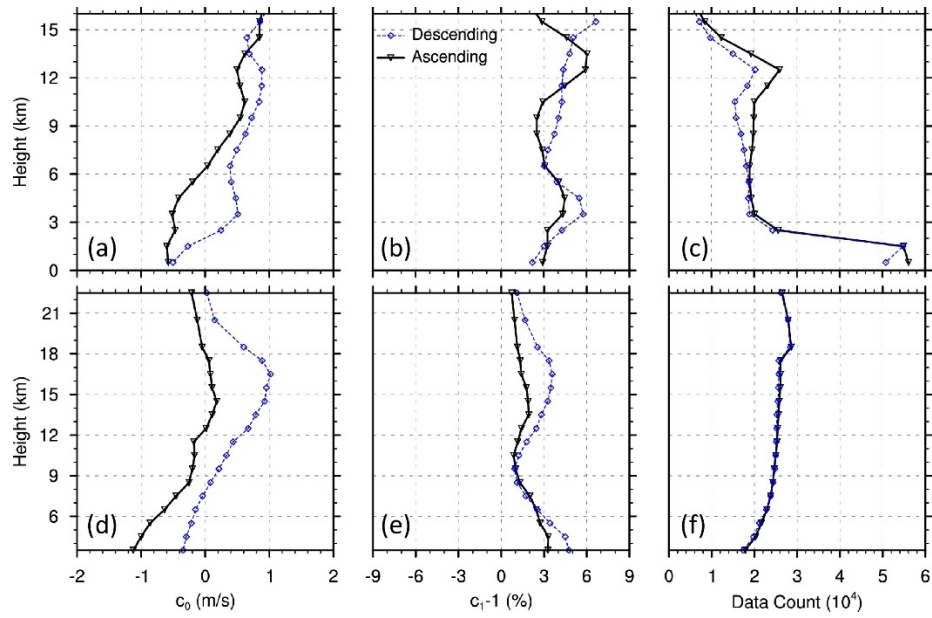
512

513 Figure 5. Density plots of global (a) Mie - FV3GFS winds in the layer at ~3.5 km altitude, and (b)  
 514 Rayleigh - FV3GFS winds in the layer at ~15 km altitude in descending orbits. The average  
 515 innovation (brown dots), the OLS regression lines of the innovations on Aeolus winds (brown),  
 516 and TLS analysis lines (blue) are shown.



517

518 Figure 6. Vertical variation of the square root of the ratio of random error variance in Mie (solid  
 519 black) and Rayleigh (dashed blue) winds versus FV3GFS winds. Results are based on global  
 520 innovations from the BASE experiment using Hollingsworth-Lonnberg method. The symbols are  
 521 plotted at the average height of the observations in each layer.



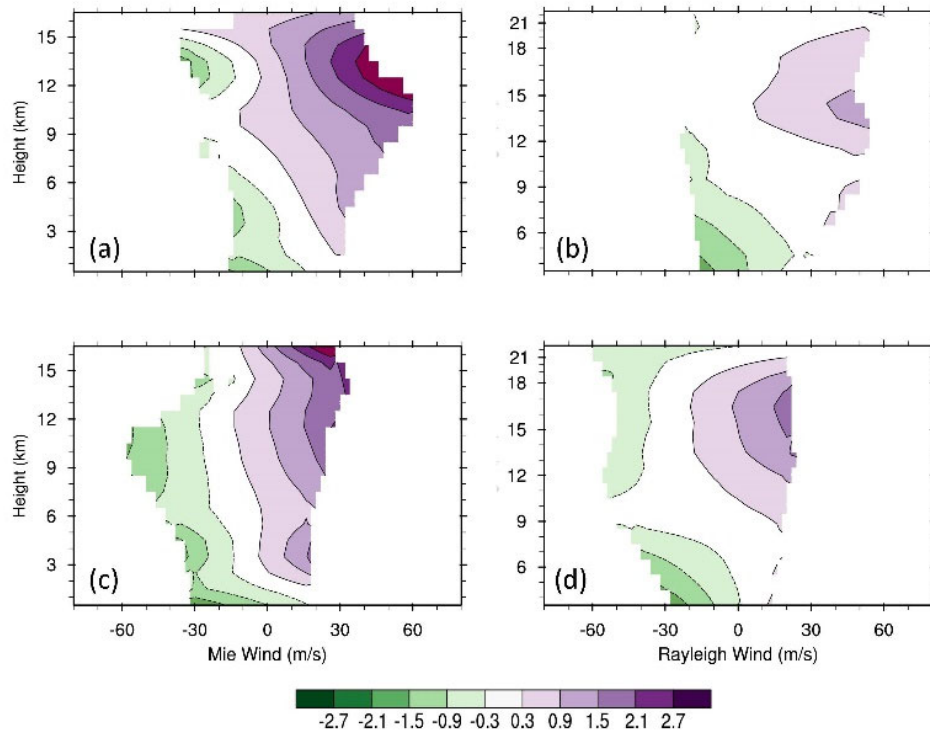
522

523 Figure 7. Vertical variations of TLS bias coefficients for Mie (a, b, c), and Rayleigh (d, e, f) winds.

524 Each point plotted represents a separate TLS analysis for all observations in each layer for all

525 latitudes and for either ascending (black solid) or descending (blue dashed) orbits. The symbols

526 are plotted at the average height of the observations in each layer.



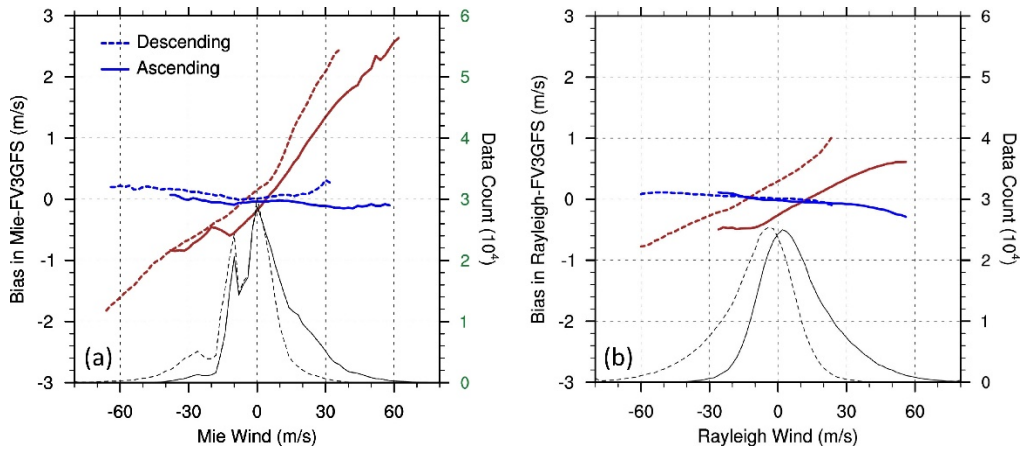
527

528 Figure 8. Vertical distributions of average TLS estimated biases (color scale, m/s) for Mie (a, c)

529 and Rayleigh (b, d) winds as a function of observed Aeolus winds (m/s) in ascending (a, b) and

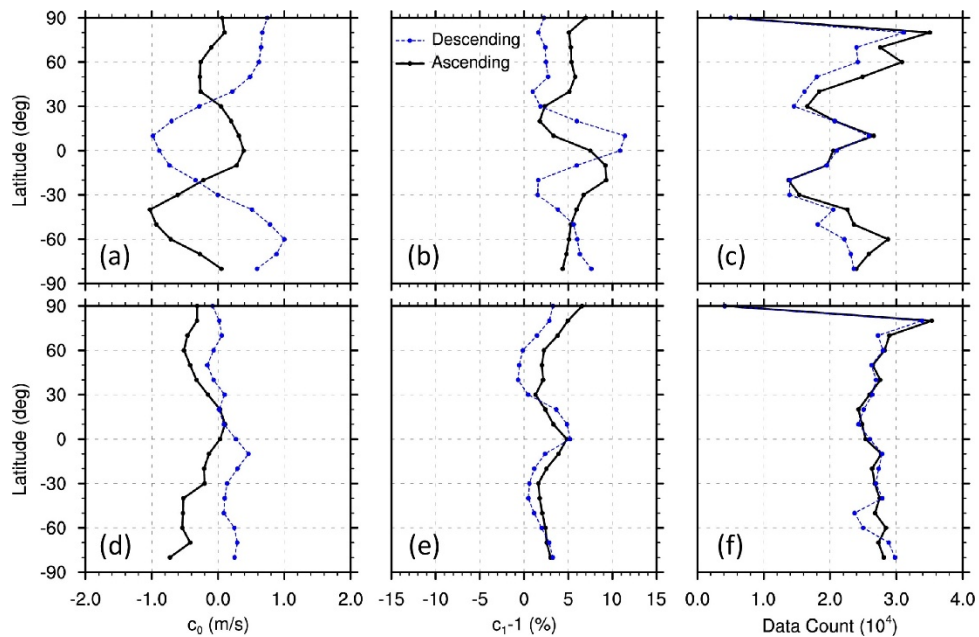
530 descending (c, d) orbits for all latitudes. The TLS estimated biases are obtained from the TLS fits

531 displayed in Fig. 7.



532

533 Figure 9. TLS estimated biases (m/s) before (brown lines) and after (blue lines) TLS bias correction  
 534 for Mie (a) and Rayleigh (b) winds as a function of the observed Aeolus winds (m/s), vertically  
 535 averaged for all latitudes of Aeolus winds. The solid and dashed lines are for ascending and  
 536 descending orbits, respectively. The black lines report the number of Aeolus winds in each 2 m/s  
 537 bin.

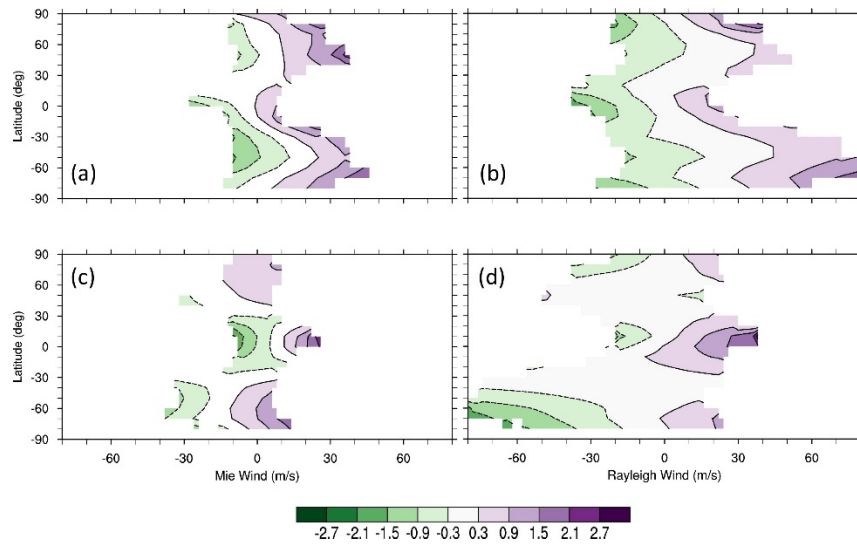


538

539 Figure 10. Latitudinal variation of TLS bias coefficients for Mie (a, b, c) and Rayleigh (d, e, f)  
 540 winds. Each point plotted represents a separate TLS analysis for all observations in all vertical

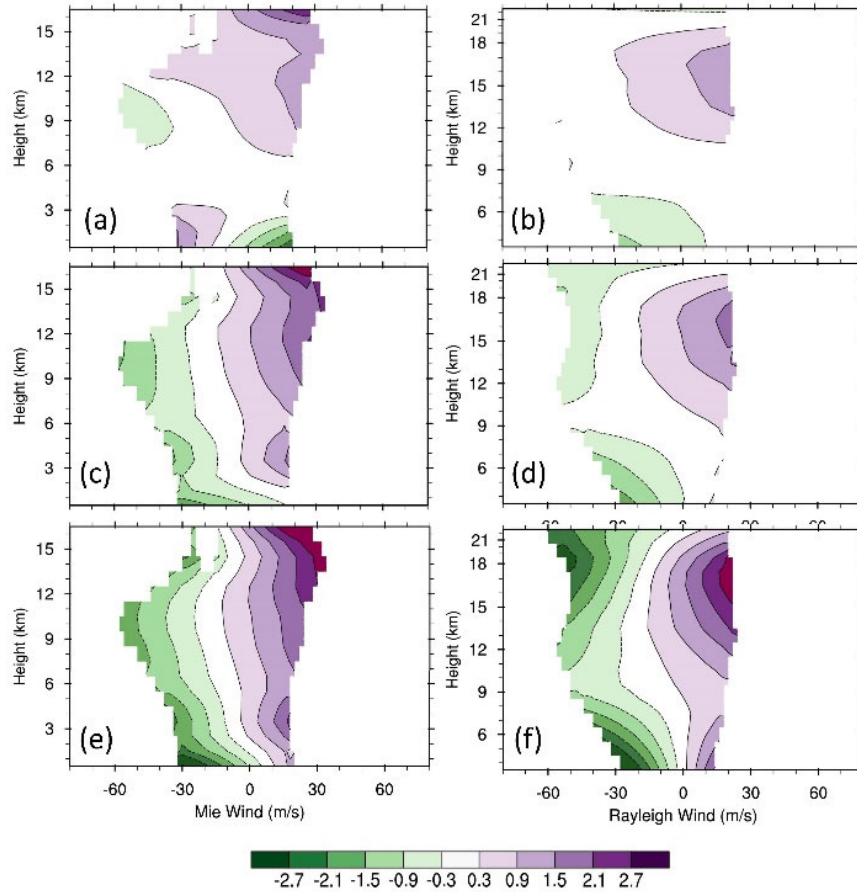
541 layers in a  $10^\circ$  latitude band for either ascending (black solid) or descending (blue dashed) orbits.  
542 The latitude bands are centered every  $10^\circ$  from  $90^\circ\text{S}$  to  $90^\circ\text{N}$ . The symbols are plotted at the center  
543 in each latitude band. The vertical layers are 0-16 km for Mie winds and 3-22 km for Rayleigh  
544 winds

545

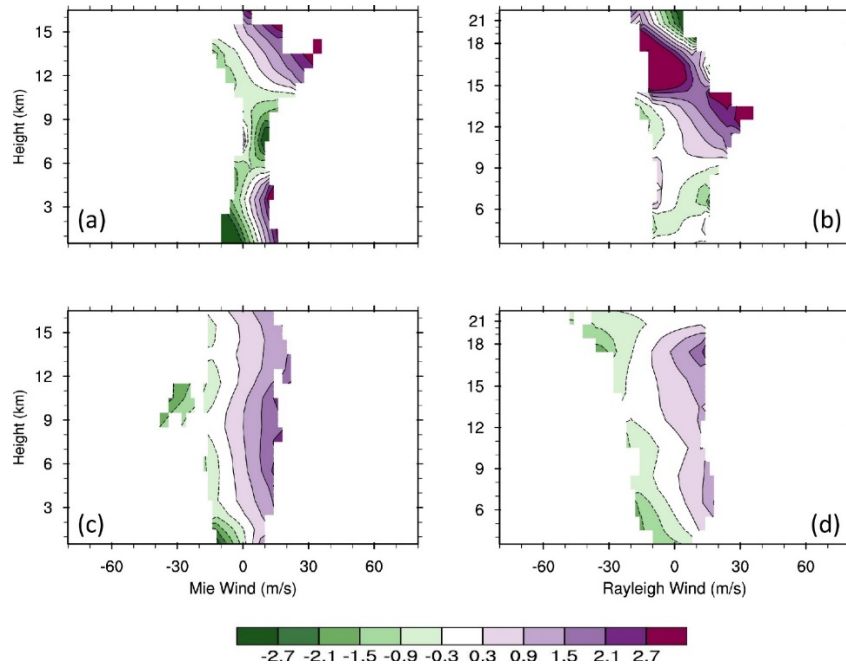


547

548 Figure 11. Latitudinal distributions of average TLS estimated biases (color scale, m/s) for Mie (a,  
 549 c) and Rayleigh (b, d) winds as a function of Aeolus wind in ascending (a, b) and descending (c,  
 550 d) orbits, obtained from the TLS fits displayed in Fig. 10.

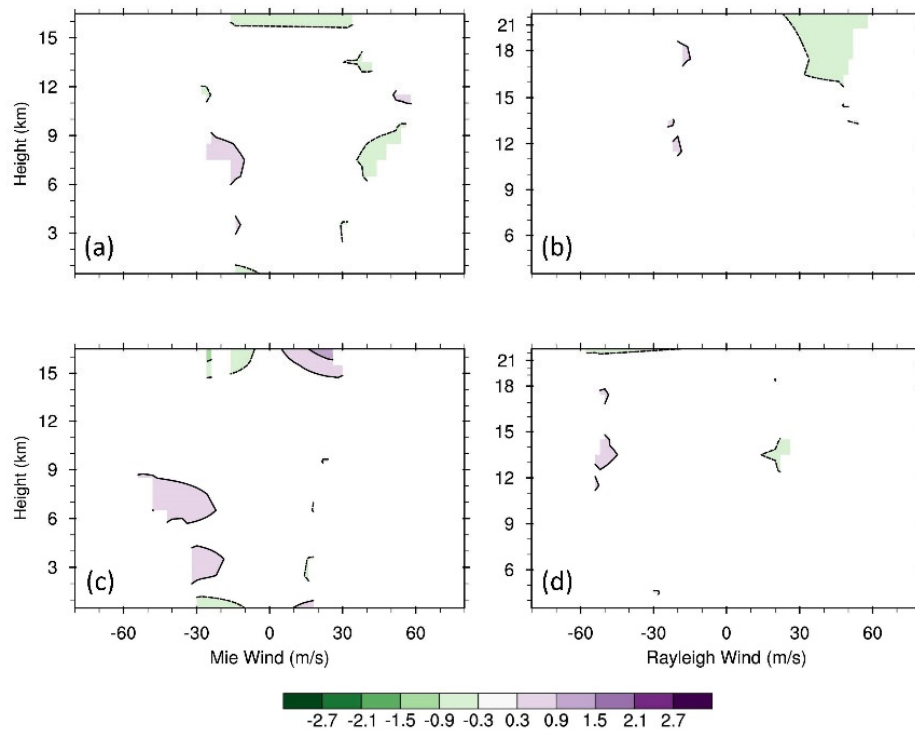


551  
 552 Figure 12. Vertical distributions of average bias estimates (color scale, m/s) for Mie (a, c, e) and  
 553 Rayleigh (b, d, f) winds as a function of Aeolus winds using one of three methods for descending  
 554 orbits for all latitudes. The methods are OLS using FV3GFS winds as a predictor (a, b), TLS (c,  
 555 d, same as the bottom panels of Fig. 8), and OLS using the average of Aeolus and FV3GFS as a  
 556 predictor (e, f).



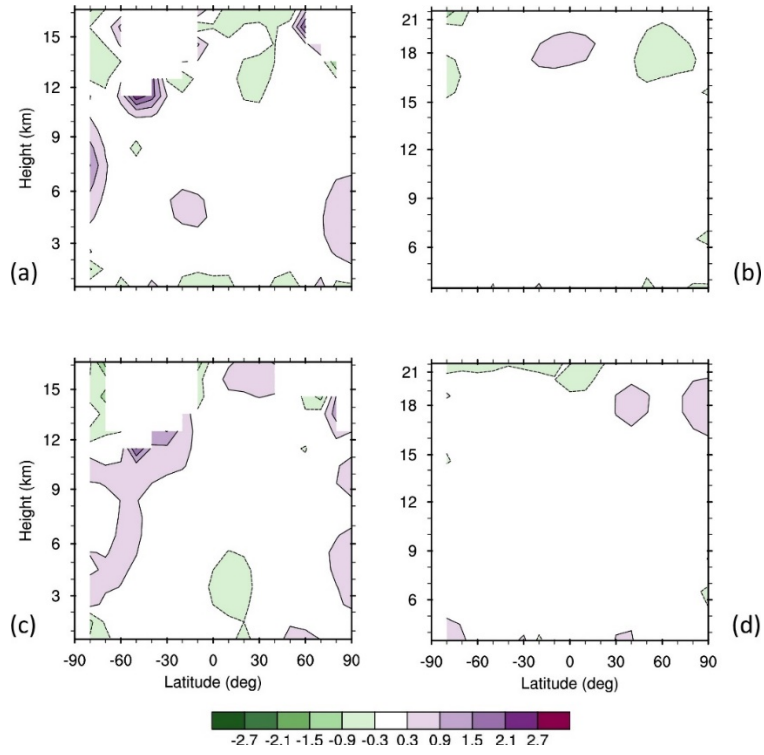
557

558 Figure 13. Vertical distributions of average TLS estimated biases (color scale, m/s) for Mie (a, c)  
 559 and Rayleigh (b, d) winds as a function of Aeolus winds (m/s) in the latitudinal bands centered at  
 560 Equator (a, b) and at 80S (c, d) for the descending orbits.



561

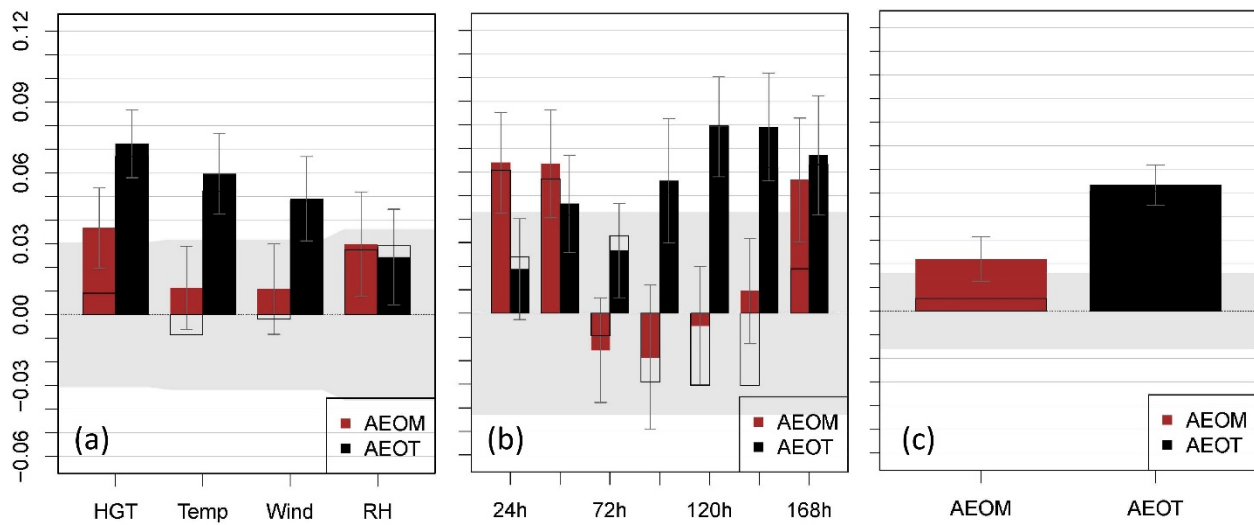
562 Figure 14. As in Fig. 8 but for the mean innovation after the TLS bias correction is applied. For  
 563 each 6-h cycle during 1-7 September 2019, the TLS bias correction is calculated from the 28  
 564 preceding 6-h cycles.



565

566 Figure 15. As in Fig. 3 but after the TLS bias correction is applied.

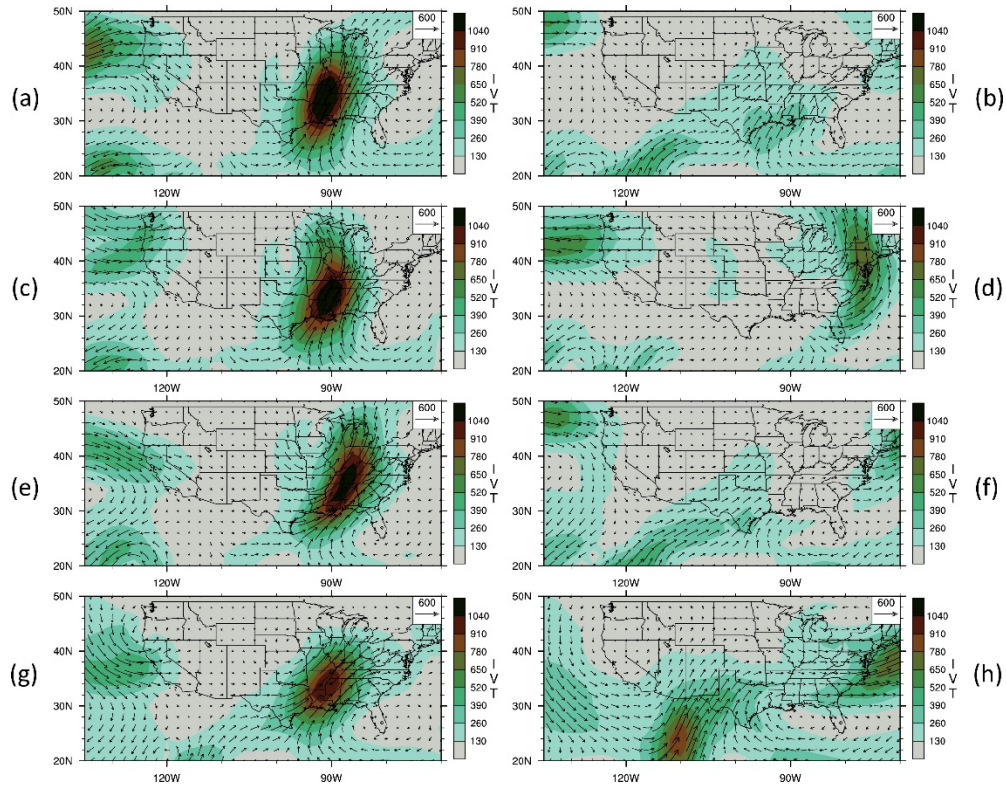
567



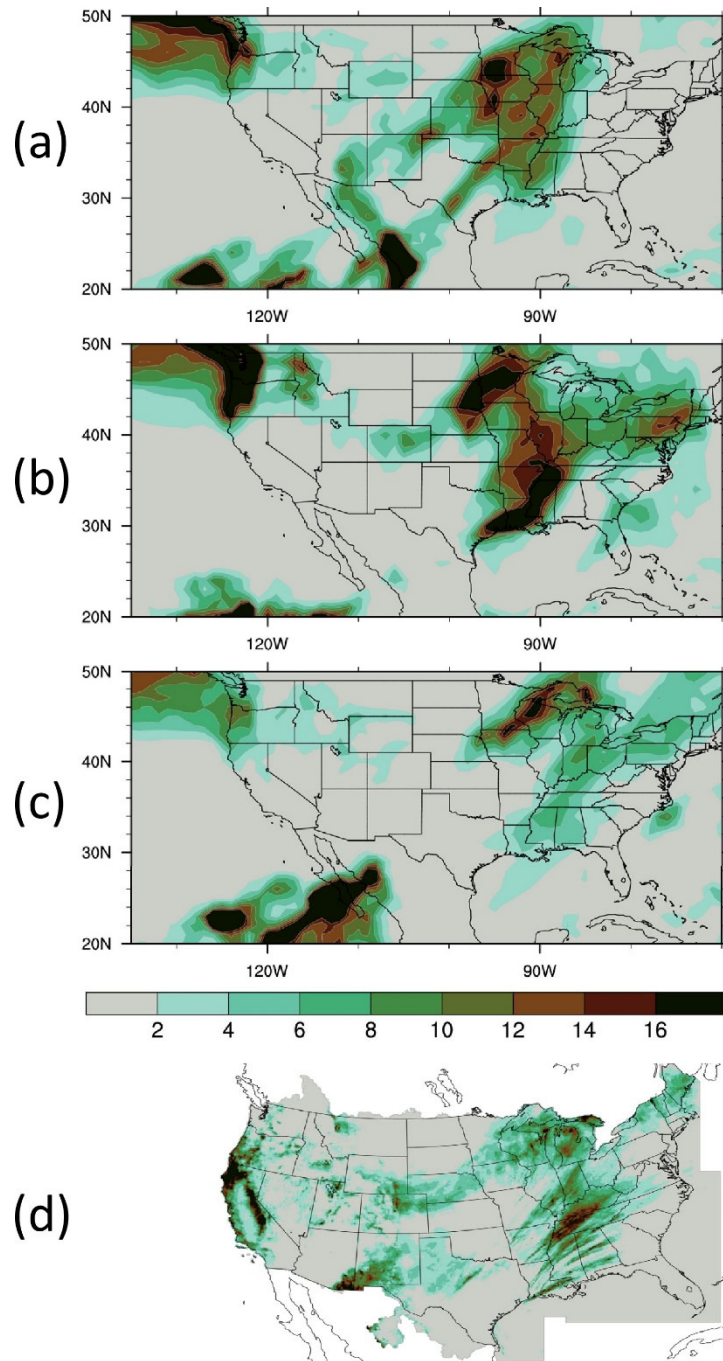
569

570 Figure 16. The Summary Assessment Metric (SAM) overall forecast scores for AEOM, and  
 571 AEOT versus BASE experiments in the North America (NA) region for Day 1-7 forecasts validated  
 572 at 0000 UTC 22-28 November 2019. The scores are shown for (a) forecast parameters of  
 573 temperature (Temp), geopotential height (HGT), vector-wind (Wind) and relative humidity  
 574 (RH), (b) lead times, and (c) overall performance of AEOM and AEOT. The forecasts are  
 575 verified to their self-analyses. Values above 0.0 demonstrate an increase in the mean of the  
 576 normalized distribution and improvement of the forecast versus the BASE, while the shaded  
 577 region represents the 95% significance level. The grey areas indicate the 95% confidence level  
 578 under the null hypothesis that there is no difference between experiments for this metric. In  
 579 addition, the estimated uncertainty at the 95% level is indicated by small error bars at the ends of  
 580 the color bars. Two normalizations are used, the ECDF (colors) and rescaled-minmax  
 581 normalization (black outline). Details in Hoffman et al. (2018). A value of 0.02, for example,  
 582 indicates the average normalized statistic over all statistics is better (greater) by 0.02 than BASE.

583 Under the null hypothesis that there are no differences, all SAMs would be 1/2, so a 0.02  
584 improvement can be considered a 4% improvement (0.02/0.5) in normalized scores.

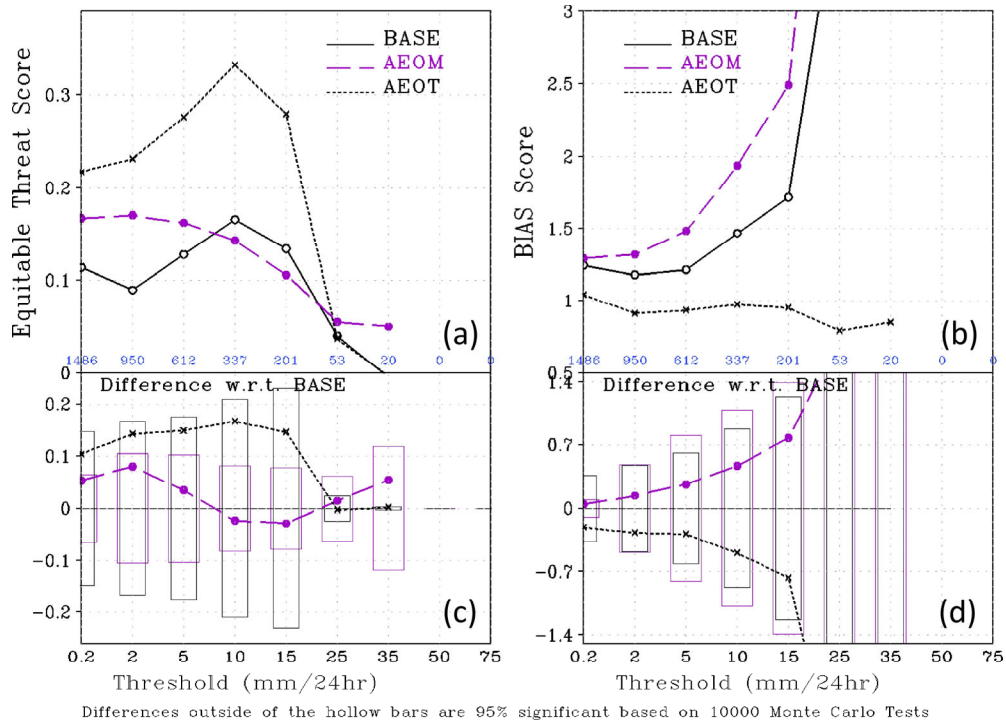


585  
586 Figure 17. The 200-1000 hPa vertically integrated water vapor transport (IVT, kg/m/s, contour)  
587 and wind vectors (m/s, arrows) in the day-7 forecasts, validated at 0000 UTC 27 (a, c, e) and 28  
588 (b, d, f) November 2019 for (a, b) BASE, (c, d) AEOM, (e, f) AEOT, and (g, h) ECMWF  
589 analyses.



590

591 Figure 18, The 24-h accumulated precipitation (mm) for 156 h to 180 h, averaged for the  
 592 forecasts validated from 1200 UTC 26 to 28 November 2019 for (a) BASE, (b) AEOM, (c)  
 593 AEOT, and (d) the NCEP precipitation raingauge data analysis.



594

595 Figure 19. The forecast skill scores for 24-h accumulated precipitation for 156 h to 180 h  
 596 forecasts validated from 1200 UTC 26 to 28 November 2019. The Equitable Threat (a) and  
 597 BIAS score (b) are measures of the forecast skill for location and amount of precipitation,  
 598 respectively. The differences relative to the BASE and the statistical significances are shown in (c) and  
 599 (d), respectively. Equitable Threat and BIAS scores closer to 1.0 indicate improved precipitation  
 600 forecast skill.